Microstructural correlations for specific surface area and triple phase boundary length for composite electrodes of solid oxide cells

Hamza Moussaoui, R.K. Sharma, Johan Debayle, Yann Gavet, Gérard Delette, Jean-Paul Laurencin

Microstructural correlations for specific surface area and triple phase boundary length for composite electrodes of solid oxide cells

H. Moussaoui[1, 2], R.K. Sharma[1], J. Debayle[2], Y. Gavet[2], G. Delette[1], J. Laurencin[1,*]

[1] Univ. Grenoble Alpes – CEA/LITEN, 38054, Grenoble, France
[2] Ecole Nationale Supérieure des Mines de Saint-Etienne, SPIN/LGF, UMR CNRS 5307, F-42023 Saint-Etienne, France

Highlights

- Microstructural correlations for specific surface area and triple phase boundary lengths.
- Calibration of the semi-analytical relationships on a large dataset of synthetic microstructures.
- Validation of the semi-analytical correlations on 3D reconstructions.

Abstract

The performances of Solid Oxide Cells (SOCs) are controlled by key microstructural properties such as the density of Triple Phase Boundary lengths (TPBl) and the interfacial specific surface areas ($S_{i/j}$). These electrode properties are dependent on basic morphological parameters defined by the phase volume fractions and the Particle Size Distributions (PSD) of the percolated solid phases. The understanding of these relationships is of central importance for designing an optimum electrode microstructure. In this study, semi-analytical expressions for the density of TPBl and the interfacial specific surface areas are investigated. For this purpose, a large number of synthetic microstructures are generated by using validated models based on the sphere packing and the truncated Gaussian random field methods. The coefficients of the parametric equations for both investigated properties (TPBl density and $S_{i/j}$) are fitted on the large database generated. The predictions of the microstructural correlations are in good agreement with the parameters directly computed on 3D reconstructions of typical LSCF-CGO and Ni-YSZ electrodes, thereby validating their reliability.

Keywords: SOFC; SOEC; triple phase boundary lengths; specific surface area; microstructural correlations.

*Corresponding author: Telephone: +33 (0)438782210, Fax: +33 (0)438784139,
E-mail: jerome.laurencin@cea.fr

1. Introduction

Solid Oxide Cells (SOCs) are electrochemical devices operating at high-temperature (700-900°C). This technology is nowadays considered as one of the most promising solutions in order to match the electricity consumption with the fluctuation of the production by the renewable energy sources. Indeed, the SOCs present a very good reversibility between fuel cells and electrolysis modes associated to a high efficiency and an excellent fuel flexibility [1-3]. However, before considering the industrial deployment of this technology, improvements in SOCs performance at lower operating temperature are still required in order to reduce the cost and to enhance the long-term durability. In this objective, several attempts have been paid to improve SOCs performance at intermediate temperature with the development of new materials and the optimization of the electrode microstructure.

Nowadays, porous materials based on Mixed Ionic Electronic Conductors (MIECs) such as Lanthanum Strontium Cobalt (LSC) or Lanthanum Strontium Cobalt Ferrite (LSCF) are commonly used as O_2 electrode in SOCs. Moreover, the addition of highly ionic conducting materials like Ceria doped Gadolinium Oxide (CGO) has recently attracted attention for improved O_2 electrode. Indeed, compared to the single solid-phase materials, the LSCF-CGO or LSC-CGO composite exhibits higher performances at intermediate temperatures and also presents a better mechanical compatibility with the classical electrolyte in Yttria Stabilized Zirconia (YSZ) [4-7]. At the present time, the porous cermet made of Nickel and YSZ is considered as the standard composite for the H_2 electrode in SOC technology. Indeed, the Ni-YSZ cermet combines a high electronic conductivity due to the Nickel with a high ionic conductivity thanks to the YSZ. It also provides a very high electrochemical activity for fuel oxidation or steam reduction as well as a good mechanical compatibility with the dense YSZ electrolyte [8,9].

The SOCs performances are highly sensitive to the complex 3D microstructure of both the H_2 and O_2 electrodes [5,10-14]. One of the key microstructural parameters is the active Triple Phase Boundaries lengths (TPBl) defined by the lines where the percolated ionic, electronic and gas phases meet. For example, the efficiency of the H_2 electrode is directly controlled by the density of active TPBl since the electrochemical reaction in the Ni-YSZ cermet takes place at these electroactive sites [8]. For the O_2 electrode, the higher performances of the LSCF-CGO

composite with respect to the pure LSCF can be explained by the extension of TPBl in the bulk of the electrode [4,5]. Indeed, it has been suggested that the oxygen oxidation/reduction at TPBl according to the so-called "surface path" could control the global electrochemical reaction for the LSCF-CGO electrode [15,16]. Aside from the TPBl, the interfacial specific surface areas $S_{i/j}$ between the electrode phases can also contribute to the global reaction mechanism (with i/j=electronic/pore, ionic/pore or electronic/ionic interfaces). For instance, it is suspected that the charge transfer at TPBl in the Ni-YSZ cermet can be co-limited by a gas interaction step with the YSZ or Ni surface [8]. For the O_2 electrode, the reaction of oxygen reduction under SOFC mode is assumed to occur on the whole LSCF/pore interfacial surface area according to the so-called "bulk path" [17,18]. In this reaction mechanism, the ionic charge transfer between LSCF and CGO is proportional to the contact surface area between the two materials.

It is also widely recognized that the electrode microstructure plays a key role on the cell durability [19-21]. For instance, the degradation mechanism in the Ni-YSZ electrode is related to the corresponding changes in the TPBl density and specific surface areas due to a microstructural evolution over time [22-25]. As the material deterioration in operation is associated to thermally activated processes, the decrease of the operating temperature should allow mitigating the degradation in performances. In this case, an electrode microstructural optimization is still necessary in order to maintain the high performances at these 'intermediate' operating temperatures. An important strategy to enhance the catalytic activity in the electrodes at lower temperatures is to increase the number of active sites via an increase in both the density of TPBl, L_{TPB}, and the specific surface areas, $S_{i/j}$, [5,11,19]. For this microstructural optimization, it is essential to link these properties to the "basic" morphological electrode parameters that can be more easily controlled by the manufacturer. These "basic" parameters correspond to (i) the porosity (θ_p), (ii) the relative phase volume fraction of solid phases ($\alpha = \theta_{io}/\theta_{ei}$) and (iii) the parameters describing the shape and the distribution of the particles (ionic and electronic conductors).

In order to establish these electrode microstructural correlations, a first strategy is based on the manufacturing of several electrodes by changing both the composition and the Particle Size Distribution (PSD) of the initial powder. The microstructural properties (L_{TPB} and $S_{i/j}$) can be measured on 3D reconstructions obtained by X-ray Computed Tomography (XCT) [26-30] or by Focused Ion Beam Scanning Electron Microscopy (FIB-SEM) [31-33]. This experimental approach requires a large number of samples for parametric studies. However, the number of

experiments is generally very limited since this method is time consuming. Therefore, the dataset is usually insufficient to fully validate the complex microstructural relationships [34,35].

An alternative approach consists in theoretical developments based on geometrical considerations. In this frame, numerical approaches can be used to derive some pure phenomenological microstructural relationships. They are based on the generation of synthetic 3D microstructures obtained by the random packing of initial spheres [36-40] or by geostatistical simulations [41-43].
In the frame of the percolation theory, analytical models are also proposed to express L_{TPB} and the specific surface area [34,44-51]. Most of these approaches are limited to mono-sized spheres with approximations on the estimation of the mean coordination number and the contact angles between the particles. Nevertheless, the microstructures of real composite electrodes are strongly disordered and the particles tend to have a complex and non-spherical shape. To overcome these issues, Gokhale et al. [35] have proposed to use the concept of "extended" microstructure and developed an analytical model for the estimation of L_{TPB} in composite electrodes taking into account the actual PSD of spheres. In this case, from our best knowledge, no correlation has been proposed for the interfacial specific surface areas.

In this work, semi-analytical expressions linking the density of TPBl and the interfacial specific surface areas to the "basic" parameters of the microstructure are studied and calibrated on two sets of synthetic 3D microstructures. These two databases have been generated by using in-house models based on the sphere packing and the truncated Gaussian random field methods. Finally, the reliability of the microstructural relationships has been checked with real 3D electrode reconstructions. The article is organized as follows: the theoretical background and the development of semi-analytical correlations are detailed in Section 2. The fitting of the parametric equations are presented and discussed in Section 3. For each property (L_{TPB} and $S_{i/i}$), the correlations deduced from simulated microstructure datasets have been compared to the data extracted from the real reconstructions in Section 4.

2. Theoretical background, development and methodology

2.1. Theoretical background

Microstructural engineering of composite electrode materials is a multivariate complex problem. Indeed, the density of TPBl and the interfacial specific surface areas, which are the key properties controlling the electrochemical response, depend on several "basic" microstructural parameters which can be linked to the powder before sintering [51]. By considering the medium described by a random packing of convex particles, these "basic" parameters of the microstructure can be ascribed to the features of the particles collection which can be defined as follows [35,52]:

(a) The phase volume fractions are expressed through the porosity (θ_p) and the ratio of the ionic to the electronic phase volume fractions ($\alpha = \theta_{io}/\theta_{el}$) with:

$$\theta_{io} + \theta_{el} + \theta_p = 1 \quad (1)$$

(b) The morphology of the electrode particles can be described for each phase *i* by two shape factors K_{1i} and K_{2i} defined by:

$$K_{1i} = \frac{\langle S_i \rangle}{\langle {D_i}^2 \rangle} \ and \ K_{2i} = \frac{\langle V_i \rangle}{\langle {D_i}^3 \rangle} with \ \text{i} = \text{ionic or electronic particles} \quad (2)$$

where D_i, S_i and V_i denote the mean diameter, the surface area and the volume for the ionic or electronic particle, respectively (note that $\langle X_i \rangle$ represents the arithmetic mean of X_i: $\langle X_i \rangle = \int_0^\infty X_i \, p(X_i) \, dX_i$ with $p(X_i)$ is the probability density function) . For the ideal case of spherical particles, the ratio $\beta_i = K_{1i}/K_{2i}$ is equal to 6 [35].

(c) The Particle Size Distribution (PSD_i) of each solid phase *i* is fully defined by the mean value $\langle D_i \rangle$, the standard deviation ${\sigma_i}^2$, the Coefficient of Variation (CV_i) and the skewness γ_i:

$${\sigma_i}^2 = \int_0^\infty [D_i - \langle D_i \rangle]^2 \, p(D_i) dD_i \ ; \ CV_i = \frac{\sigma_i}{\langle D_i \rangle}; \ \gamma_i = \frac{1}{{\sigma_i}^3} \int_0^\infty [D_i - \langle D_i \rangle]^3 \, p(D_i) dD_i \quad (3)$$

Therefore, the density of TPBl and the interfacial specific surface areas have to be expressed as a function of θ_p, $\alpha, \beta_i, \langle D_i \rangle$, CV_i and γ_i.

As mentioned in the introduction, phenomenological equations can be derived from the generation of synthetic microstructures obtained by geometrical stochastic simulations (based on the random packing of particles or geostatistical modelling). As a general matter, these methods require intensive computational means for the generation of a large dataset of 3D microstructures and must also involve complex optimization algorithms of data mining [53].

Aside from these numerical computations, some analytical developments based on the percolation theory have been proposed to establish the microstructural correlations. Most of them are focused on the density of TPBl [34,44-46,48-51], while Chen et al. [34] and Costamagna et al. [47] have dealt with the interfacial specific surface area between the electronic/pore and ionic/electronic phases, respectively. All these mathematical models, which are based on pure geometrical considerations, are free from the computational cost of 3D simulations but require some simplifications. All these models consider spherical particles for the electronic and ionic conductors which are loosely packed. The particles of each constituent have the same coordination number while the distance between the particle centers (or the contact angle) depicting the spheres intersection is constant. In the first studies, the spheres of each phase were assumed to have the same size [45,47,49]. This simplification has been recently improved by extending the modelling to poly-dispersed particles [34,44,46,48,51]. Nevertheless, they still do not capture the effects of particle shapes/morphologies and the distribution on the coordination number. However, a distribution of the coordination number is expected in real microstructures exhibiting a scattering on the particle size. Indeed, there is a clear correlation between the particle size and the number of bonds in the lattice. Moreover, a distribution on the contact angles related to the particles intersection could also affect the distribution on the coordination number. Finally, it is worth noting that all these models rely on the knowledge of the particles intersection and/or the coordination number. Nevertheless, the definition and the computation of these properties for real partially sintered microstructures is not straightforward and requires further simplifying assumptions [35].

To overcome these issues, Gokhale et al. [35] have proposed a stochastic geometry based analytical expression for the total L_{TPB} related to the overall phases (i.e. including the percolated phases and the disconnected clusters). The model is applicable for particles of any convex shapes and size distribution. For this purpose, they have used the notion of "extended" microstructure, widely employed in modeling phase transformations [54-60]. With such an approach, the effects of the particle shape and size distribution can be taken into account:

$$L_{TPB} = \frac{\pi}{4}\frac{\alpha}{(1+\alpha)^2}\theta_p\left(ln\theta_p\right)^2\beta_{io}\beta_{el}\frac{1}{\langle D_{io}\rangle\langle D_{el}\rangle}\frac{\left(1+{CV_{io}}^2\right)}{\left(1+3{CV_{io}}^2+\gamma_{io}{CV_{io}}^3\right)}\frac{\left(1+{CV_{el}}^2\right)}{\left(1+3{CV_{el}}^2+\gamma_{el}{CV_{el}}^3\right)} \qquad (4)$$

As seen in the previous equation, the density of total TPBl is then explicitly expressed as a function of the 'basic' parameters of the microstructure. The consistency of this theoretical relation has been checked by Zhang et al. [61] thanks to 3D simulated volumes generated by an algorithm developed to produce the same microstructure as defined in the analytical model. As

expected, they have found a very good agreement between the simulated and predicted TPBl. They have also checked that eq. (4) stands to accurately predict the active density of TPBl as long as the electrode phases are well connected (i.e. solid phase volume fraction higher than 30 % and porosity higher than 10% in their case).

2.2 Theoretical development: analytical expression for $S_{i/j}$ and S_i

In this work, we have derived the analytical expressions for the interfacial specific surface areas $S_{i/j}$ as a function of the microstructural parameters of the composite electrode. The electrode specific surface areas S_p can be obviously deduced from the former relations with $S_p = S_{io/p} + S_{el/p}$. The same procedure as the one proposed by Gokhale et al. [35] for the density of TPBl has been followed. The main steps of this study are detailed hereafter.

2.2.1. Concept of "extended" microstructure

The approach is based on the concept of a virtual domain called the "extended" microstructure [54-56]. In this domain, the centers of convex particles are randomly distributed by a homogeneous Poisson point process. The ionic and electronic particles in the "extended" microstructure are free to interpenetrate while the remaining empty space corresponds to the porosity (Fig. 1). With such a definition, the volumes of the ionic and electronic phases are overestimated in the "extended" domain since the particles cannot overlap in the "real" microstructure. Nevertheless, the properties of the "actual" microstructure can be deduced from the virtual domain by taking into account the particles overlap. Indeed, only a fraction of any incremental volume change in the "extended" microstructure dV_i^{ex} contributes to a change in the real microstructure dV_i (the subscript *i* denotes the ionic or electronic phase). Assuming that the particles are randomly distributed, this fraction of dV_i^{ex} corresponds to the volume in the extended microstructure which is formed in the complementary phase of the solid particles (i.e. the porosity); whereas the volume that drops within the overlap must be ignored (Fig. 1). On average, any increment of volume in the real medium is thus proportional to the volume increase in the extended microstructure as follows [60]:

$$dV_{el} = \left[1 - \frac{V_{el} + V_{io}}{V_{tot}}\right] dV_{el}^{ex} \quad and \quad dV_{io} = \left[1 - \frac{V_{el} + V_{io}}{V_{tot}}\right] dV_{io}^{ex} \tag{5}$$

where V_{tot} denotes the volume of the considered domain. The terms V_i and V_i^{ex} are related to the volumes of the phase *i* for the extended and real microstructures, respectively. Knowing that

$\frac{\theta_{io}}{\theta_{el}} = \alpha$ (where θ_i and represents the phase volume fraction with $\theta_{io} = \frac{V_{io}}{V_{tot}} and\ \theta_{el} = \frac{V_{el}}{V_{tot}}$). Jones and Bhadeshia [60] have integrated the increment of volumes to find the relations between the extended and real volumes for two phases:

$$\frac{V_{el}^{ex}}{V_{tot}} = \frac{-1}{1+\alpha} ln\left[1-(1+\alpha)\frac{V_{el}}{V_{tot}}\right] \quad and \quad \frac{V_{io}^{ex}}{V_{tot}} = \frac{-\alpha}{1+\alpha} ln\left[1-\left(\frac{1+\alpha}{\alpha}\right)\frac{V_{io}}{V_{tot}}\right] \tag{6}$$

It can be noticed that the two previous relations in eq. (6) imply that:

$$\frac{\theta_{io}^{ex}}{\theta_{el}^{ex}} = \frac{\theta_{io}}{\theta_{el}} \tag{7}$$

The combination of eq. (6) and eq. (1) allows the volume fraction of the ionic and electronic conductors in the extended microstructure to be expressed as a function of the porosity of the real medium:

$$\theta_{el}^{ex} = \frac{-1}{1+\alpha} ln[\theta_p] \quad and \quad \theta_{io}^{ex} = \frac{-\alpha}{1+\alpha} ln[\theta_p] \tag{8}$$

These last equations will be used to express the interfacial specific surface areas.

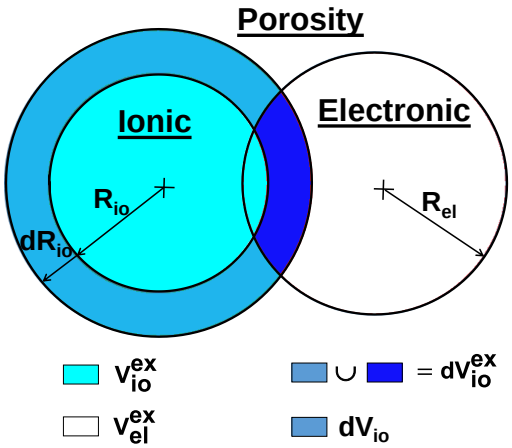

Fig. 1: Schematic representation of two overlapping particles in the "extended" microstructure (given here for two spherical particles in ionic and electronic conducting phases).

2.2.2. Specific surface area in the "real" and "extended" microstructures for the ionic/pore and electronic/pore interfaces

In the following, S_{io}^{ex} and S_{el}^{ex} denote the specific surface areas for the ionic and electronic phases in the extended microstructure, whereas $S_{io/p}$ and $S_{el/p}$ represent the interfacial surface areas per unit volume of sample between the ionic/porosity and electronic/porosity phases in the corresponding real microstructure. As previously discussed for the volumes, only a part of the

surface area in the extended microstructure can contribute to the surface area in the real microstructure. By analogy with the volume increments in eq. (5), the interfacial surface area of the ionic or electronic particles in contact with porosity in the real microstructure is only equal to the fraction of the surface area that falls within the porosity in the extended microstructure. As a consequence, it can be shown starting from eq. (5) [58,59] the following relations:

$$S_{el/p} = \theta_p S_{el}^{ex} \quad and \quad S_{io/p} = \theta_p S_{io}^{ex} \tag{9}$$

These last equations will be used to express the interfacial specific surface areas as a function of the geometrical characteristics of the electrode phases.

2.2.3 Expression of the ionic/pore and electronic/pore interfacial specific surface areas versus the "basic" electrode microstructural parameters

The specific surface area for each solid phase in the extended microstructure, S_{el}^{ex} or S_{io}^{ex}, is directly given by the mean surface area of the electronic or ionic particles, $\langle S_{el} \rangle$ or $\langle S_{io} \rangle$, multiplied by the number of particles per unit volume, N_{el} or N_{io}:

$$S_{el}^{ex} = N_{el} \langle \mathrm{S_{el}} \rangle \quad and \quad S_{io}^{ex} = N_{io} \langle \mathrm{S_{io}} \rangle \tag{10}$$

The same relations can be also written for the volume fractions in the extended microstructure:

$$\theta_{el}^{ex} = N_{el} \langle V_{el} \rangle \quad and \quad \theta_{io}^{ex} = N_{io} \langle V_{io} \rangle \tag{11}$$

Where $\langle V_{el} \rangle$ and $\langle V_{io} \rangle$ denote respectively the mean value for the volume of the electronic and ionic particles. For each solid phase, the combination of eq. (9) to (11) yields the following expressions:

$$S_{el/p} = \theta_p \frac{\langle S_{el} \rangle}{\langle V_{el} \rangle} \theta_{el}^{ex} \quad and \quad S_{io/p} = \theta_p \frac{\langle S_{io} \rangle}{\langle V_{io} \rangle} \theta_{io}^{ex} \tag{12}$$

The relations given in eq. (8) can be introduced in eq. (12) in order to express the interfacial specific surface area with the parameters of the "real" microstructure only:

$$S_{el/p} = \frac{-1}{1+\alpha} \theta_p ln[\theta_p] \frac{\langle S_{el} \rangle}{\langle V_{el} \rangle} \quad and \quad S_{io/p} = \frac{-\alpha}{1+\alpha} \theta_p ln[\theta_p] \frac{\langle S_{io} \rangle}{\langle V_{io} \rangle} \tag{13}$$

The first terms in eq. (13) describe the variation of the interfacial specific surface areas with the volume fractions of the three ionic, electronic, and pore phases. The ratio, $\frac{\langle S_{el} \rangle}{\langle V_{el} \rangle}$ or $\frac{\langle S_{io} \rangle}{\langle V_{io} \rangle}$, is related to the morphology of the electronic or ionic particles. Indeed, by using eq. (2), the ratio can be replaced by the mean diameter and the shape factor of particles as follows:

$$S_{el/p} = \frac{-1}{1+\alpha} \theta_p ln[\theta_p] \beta_{el} \frac{\langle {D_{el}}^2 \rangle}{\langle {D_{el}}^3 \rangle} \quad and \quad S_{io/p} = \frac{-\alpha}{1+\alpha} \theta_p ln[\theta_p] \beta_{io} \frac{\langle {D_{io}}^2 \rangle}{\langle {D_{io}}^3 \rangle} \tag{14}$$

The ratio, $\beta_{el}=K_{1el}/K_{2el}$ or $\beta_{io}=K_{1io}/K_{2io}$, depends only on the electronic or ionic particle shape whereas the last term, $\frac{\langle {D_{el}}^2 \rangle}{\langle {D_{el}}^3 \rangle}$ or $\frac{\langle {D_{io}}^2 \rangle}{\langle {D_{io}}^3 \rangle}$, contains the characteristics describing the particle size distribution. Indeed, with the definitions of the standard deviation ${\sigma_i}^2$, the coefficient of variation CV_i and the skewness γ_i given in eq. (3), it can be shown that:

$$\langle {D_i}^2 \rangle = \langle D_i \rangle^2 \left[1 + {CV_i}^2\right] \quad and \quad \langle {D_i}^3 \rangle = \langle D_i \rangle^3 \left[1 + 3{CV_i}^2 + \gamma_i {CV_i}^3\right] \tag{15}$$

Finally, the combination of eqs. (15) and (14) allows the surface areas versus the "basic" microstructural parameters of the electrode to be expressed for both the electronic/porosity and ionic/porosity interfaces:

$$S_{el/p} = \frac{-1}{1+\alpha}\theta_p ln\left[\theta_p\right]\beta_{el}\frac{1}{\langle D_{el}\rangle}\frac{\left[1+{CV_{el}}^2\right]}{\left[1+3{CV_{el}}^2+\gamma_{el}{CV_{el}}^3\right]} \tag{16a}$$

$$S_{io/p} = \frac{-\alpha}{1+\alpha}\theta_p ln\left[\theta_p\right]\beta_{io}\frac{1}{\langle D_{io}\rangle}\frac{\left[1+{CV_{io}}^2\right]}{\left[1+3{CV_{io}}^2+\gamma_{io}{CV_{io}}^3\right]} \tag{16b}$$

It is worth reminding that the "extended" microstructure is composed of ionic and electronical particles while the porosity is taken as the complementary phase (Fig. 1). With such a configuration, the contact surface between two overlapping particles is not well defined. Therefore, the same development cannot be applied to derive the formula expressing the interfacial specific surface area between the electronic and ionic particles $S_{io/el}$. From that point of view, further assumptions are required.

2.2.4 Expression of the interfacial specific surface area between the ionic and electronic phases

With simple geometrical considerations, it can be shown that the surface area $S_{io/el}$ is linked to the density of TPBl. Indeed, the interfacial surface area between two convex ionic and electronic particles is proportional to the contact perimeter.

Assuming spherical particles, the density of TPBl is simply given by the number of ionic and electronic contacts per unit volume, N_c, multiplied by the mean circumference of the intersections:

$$L_{TPB} = N_c \pi \langle d_c \rangle \tag{17}$$

where $\langle d_c \rangle$ is the mean value of the contact diameter between the ionic and electronic particles. Accordingly, the interfacial specific surface area can be expressed as $S_{el/io} = a_1 \times N_c \pi \langle d_c \rangle^2/4$ where the term a_1 is a factor of proportionality taking into account a potential roughness of the

solid/solid interface created during the sintering. The interfacial specific surface area between the electronic and ionic particles is then given by:

$$S_{el/io} = a_1 \times L_{TPB}\langle d_c \rangle / 4 \tag{18}$$

Considering the geometry of a Hertzian contact force model for spheres, Amitai et al. [62] have shown that $\langle d_c \rangle$ can be related to the mean diameters of the ionic and electronic particles:

$$\frac{\langle d_c \rangle^2}{4} \approx \frac{\langle D_{el} \rangle \langle D_{io} \rangle}{\langle D_{el} \rangle + \langle D_{io} \rangle} \ell \tag{19}$$

where ℓ denotes the penetration length of the particles intersection. Unfortunately, this parameter depends on the local geometry of the intersections (contact angle and sphere radius). However, it varies over a limited range for "classical" electrode microstructures with a good estimation given by $\ell = a_2 \times \min\{\langle D_{el} \rangle, \langle D_{io} \rangle\}$, where a_2 is a constant of proportionality depending on the mean contact angle $\langle \Theta \rangle$. This approximation is rigorously fulfilled when the ionic and the electronic particles have the same size. Indeed, the penetration length is then simply given by $\ell = a_2 \times \langle D_{i=io\ or\ el} \rangle$ (with $a_2 = (1 - cos\langle \Theta_{i=io\ or\ el} \rangle)$). However, this relation is also valid when one of the mean phase diameters is significantly higher than the other (in this case, $\ell = a_2 \times \min\{\langle D_{el} \rangle, \langle D_{io} \rangle\}$. Therefore, by combining (4), (18) and (19), the interfacial specific surface area between the ionic and electronic phases can be given as a function of the geometrical attributes of the microstructure:

$$\begin{aligned} S_{el/io} = \frac{\pi}{8} \frac{\alpha}{(1+\alpha)^2} \theta_p (ln\theta_p)^2 \frac{\beta_{io}\beta_{el} a}{\sqrt{\max\{\langle D_{el} \rangle, \langle D_{io} \rangle\} \times (\langle D_{io} \rangle + \langle D_{el} \rangle)}} \\ \times \frac{\left(1 + {CV_{io}}^2\right)}{\left(1 + 3{CV_{io}}^2 + \gamma_{io} {CV_{io}}^3\right)} \frac{\left(1 + {CV_{el}}^2\right)}{\left(1 + 3{CV_{el}}^2 + \gamma_{el} {CV_{el}}^3\right)} \end{aligned} \tag{20}$$

where a is a constant of proportionality (depending on a_1 and a_2). As for the TPBl, this correlation is expressed for the whole ionic/electronic surface area including the connected and disconnected phases. However, it must be still valid for the connected phases as long as all the electrode phases are above the percolation threshold.

2.3 Methodology for calibrating and validating the microstructural correlations

2.3.1 Calibration of the semi-analytical correlations

The "basic" microstructural parameters used in the correlations are associated to the geometric attributes that describe the morphology of the electrode particles collection. If the sintering temperature is not too high, these parameters must not be too far from the geometrical

characteristics of the initial powders [51]. However, the full relevance of this claim is questionable as the solid phases in real electrodes exhibit a continuous shape with no remanence of the initial geometry of the powder particles [9,41,42]. Nevertheless, considering the real electrodes, the "basic" microstructural parameters can still be measured by image analysis on 3D reconstructions (or assessed on 2D micrographs with stereological assumptions). For example, the parameters $\langle D_i \rangle$, CV_i and γ_i can be measured using the concept of continuous PSD [63]. Therefore, only the determination of the ratio β_{el}, β_{io} and the parameter a is not straightforward.

In the present work, the correlations have been calibrated thanks to the generation of a large database of representative 3D synthetic microstructures. In other words, the unknown parameters β_{el}, β_{io} and a of the correlations have been fitted on the numerical dataset computed on the 3D volumes. Besides, the consistency of the microstructural correlations have been checked by varying independently (i) the electrode composition, (ii) the porosity and (iii) the mean particle size of the ionic and electronic phases (which constitute the main parameters that can be easily adapted for an electrode microstructural optimization).

2.3.2 Generation of the synthetic microstructures

It is worth noting that a special attention has been paid to generate synthetic microstructures which are representative of the morphology of real typical SOC electrodes. In practice, two distinct 3D stochastic models for the generation of synthetic microstructures have been used. Both methods and their validation have been detailed elsewhere [41,64]. The first method is based on an original sphere-packing algorithm [64] shortly described hereafter. The empty volume is firstly divided in sub-domains in which initial spheres are randomly positioned. Then, in order to fill the space, new spheres are added in an iterative process up to reach the targeted electrode density. In the procedure, both distributions in the particle size and their overlapping are controlled. Finally, the microstructure is smoothed with a specific geometrical operation (morphological opening) to remove the unrealistic spherical shapes of the solid phases. The second method is based on a geostatistical modelling approach where the microstructure is simulated using morphological functions. In our case, the truncated plurigaussian random field method has been adapted to simulate the SOCs electrode microstructures [41]. Basically, two Gaussian random noises are independently convoluted with two distinct weight functions that contain the statistical information of the composite

electrode to mimic. The resulting correlated bigaussian field is then thresholded to obtain the final microstructure.

The representativeness of the two models [41,64] has been checked on the same 3D reconstruction of a typical Ni-YSZ cermet [28] used as reference for the database generation (named Electrode_1 in the article). It can be noticed that, being radically different, both approaches lead to produce distinct microstructures even if they have to emulate the same porous medium. Therefore, the two models must provide two approximations of the real microstructures, and hence, two approximations for the correlations calibrated on the two numerical datasets.

2.3.3 Validation of the microstructural correlations

Finally, the validity of the correlations to predict the microstructural properties has been checked thanks to various reconstructions acquired on different electrodes. In this frame, the reconstruction of a second typical cermet published in [41] has been used. Besides, a typical O_2 electrode made of LSCF and CGO (Electrode_3) has been specifically reconstructed by FIB-SEM according to the protocol detailed in [32]. The ability of the correlation to reproduce the loss of TPBl after Ni agglomeration has also been checked on Electrode_1 thanks to 3D volumes reconstructed after long-term operation [25].

2.3.4 Visualization of the real and synthetic electrodes microstructures

The 3D rendering volumes of the three electrode reconstructions are provided in Fig. 2. The synthetic microstructures (digital twins) generated by the sphere-packing and the random fields methods are also given for Electrode_1 taken as reference for the sensitivity analysis. The simulated volumes obtained by changing the electrode porosity are also provided as an illustration. A volume of 15x15x15 μm^3 with a resolution of 50 nm is taken for the synthetic microstructures. As already discussed in Mousaoui et al. [41], this size of the 3D volume is sufficiently large to reach a good representativeness of the heterogeneous electrode microstructure (so that it can be considered as a Representative Volume Element (RVE) of the microstructure for which only one realization is required).

The microstructural properties have been measured on the synthetic microstructures or real reconstructions thanks to a set of in-house programs already detailed in [14,41,65]. It can be noticed that, in our case, the continuous PSD is computed according to the procedure given in Gelb et al. [66]. It is defined by the probability that a voxel belongs to the largest sphere that does not overlap any complementary phase [14,66]. For the continuous shape of the real electrode phase (Fig. 2), it is reminded that the parameters describing the distribution are thus not related to a collection of discrete particles. As a consequence, the ratios β_{el}, β_{io} and the parameter a for the sintered SOC electrodes cannot be directly associated to the geometrical shapes of distinct particles. In the present work, the parameters $\beta_{el}, \beta_{io}, a$ are thus fitted on the 3D microstructures, in such a way that the relationships for L_{TPB} and $S_{i/j}$ given by eqs (4), (16) and (20) can be seen as semi-analytical correlations.

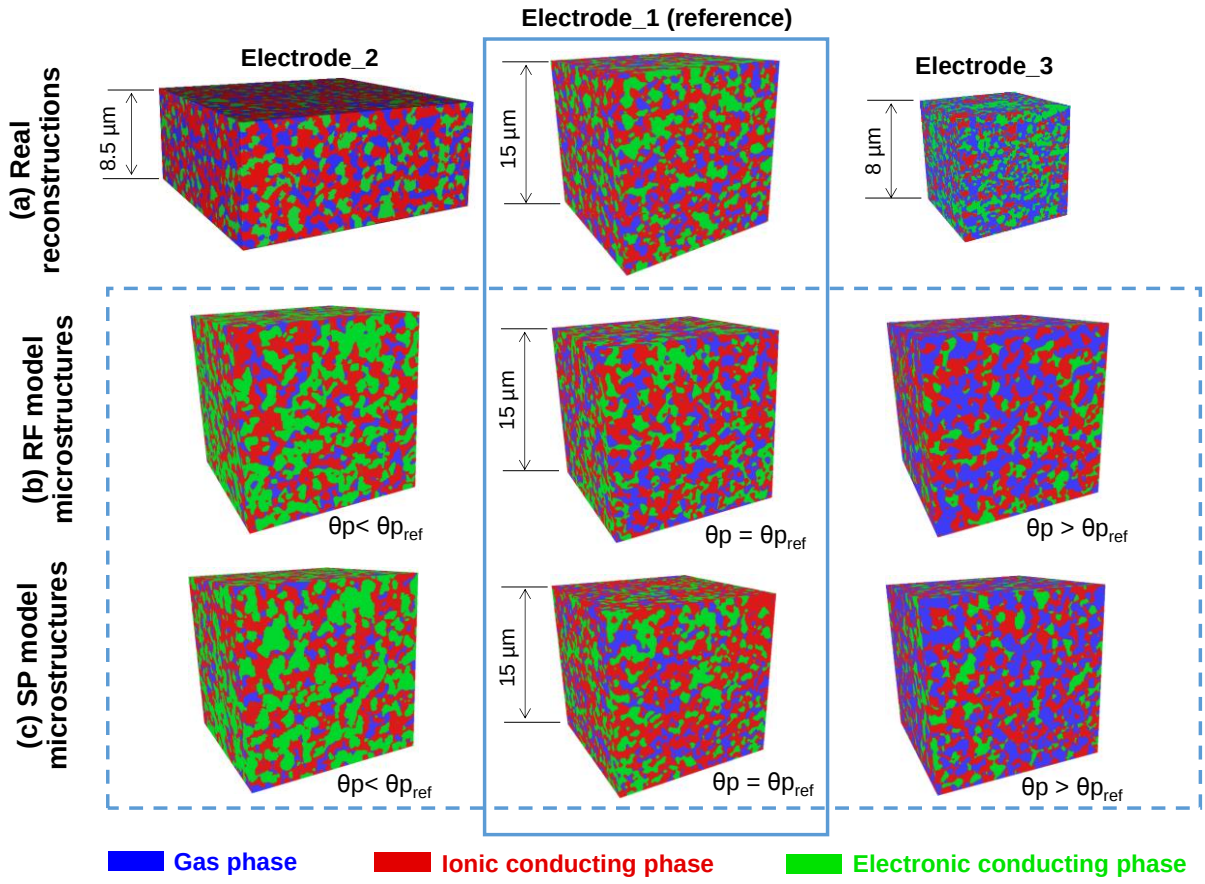

Fig. 2: (a): 3D rendering volumes for the reconstructions of Electrode_1 (Ni-YSZ), Electrode_2 (Ni-YSZ) and Electrode_3 (LSCF-CGO). (b) and (c): the synthetic microstructures of Electrode_1 generated by the Gaussian random field and the sphere packing models are shown with a sensitivity analysis on the porosity.

3. Calibration of the microstructural correlations

3.1 Correlations for the electronic/pores and ionic/pores interfacial specific surface area

As the correlations have been established for the specific surface area including the connected and disconnected phases, they have been calibrated on the 3D microstructures taking into account the total phases. However, the analyses have been conducted over a range of porosities and composition for which each phase remains almost fully percolated. In practice, the fitting procedure has been performed while keeping the electrode porosity and the ionic and electronic volume fractions higher than the phase percolation threshold (around 18%). Over this range of electrode compositions, the phase percolation remains higher than 93% so that the correlations should be still valid if considering only the connected phases. The full validity of this last assumption has been *a posteriori* verified by comparing the predicted surface area with the data obtained on the percolated phases.

3.1.1 Ionic/pores interfacial specific surface area

The ionic/pores interfacial surface area $S_{io/p}$ calculated with eq. (16b) is compared to the numerical values computed on the 3D microstructures by changing the porosity θ_p, the composition $\alpha = \theta_{io}/\theta_{el}$ and the mean phase diameters $\langle D_{io} \rangle$ and $\langle D_{el} \rangle$ in Fig. 3a, 3b and 3c, respectively. As a general comment, a good agreement is observed between the whole numerical dataset, generated either with the Random Field (RF) model or the Sphere Packing (SP) model, and the semi-analytical correlation (16b) for which only one scaling parameter β_{io} has been fitted.

As previously mentioned, some specific surface areas have also been calculated on the 3D microstructures by considering only the connected phases. These computations have been performed for the microstructural parameters taken at three bounds in the sensitivity analysis: pores, Ni or YSZ volume fractions equal to 18%. As expected, it can be seen in Fig. 3 that the

bias, which is introduced with only the percolated phases, remains negligible (as long as the phase volume fractions are not lower than ≈18%).

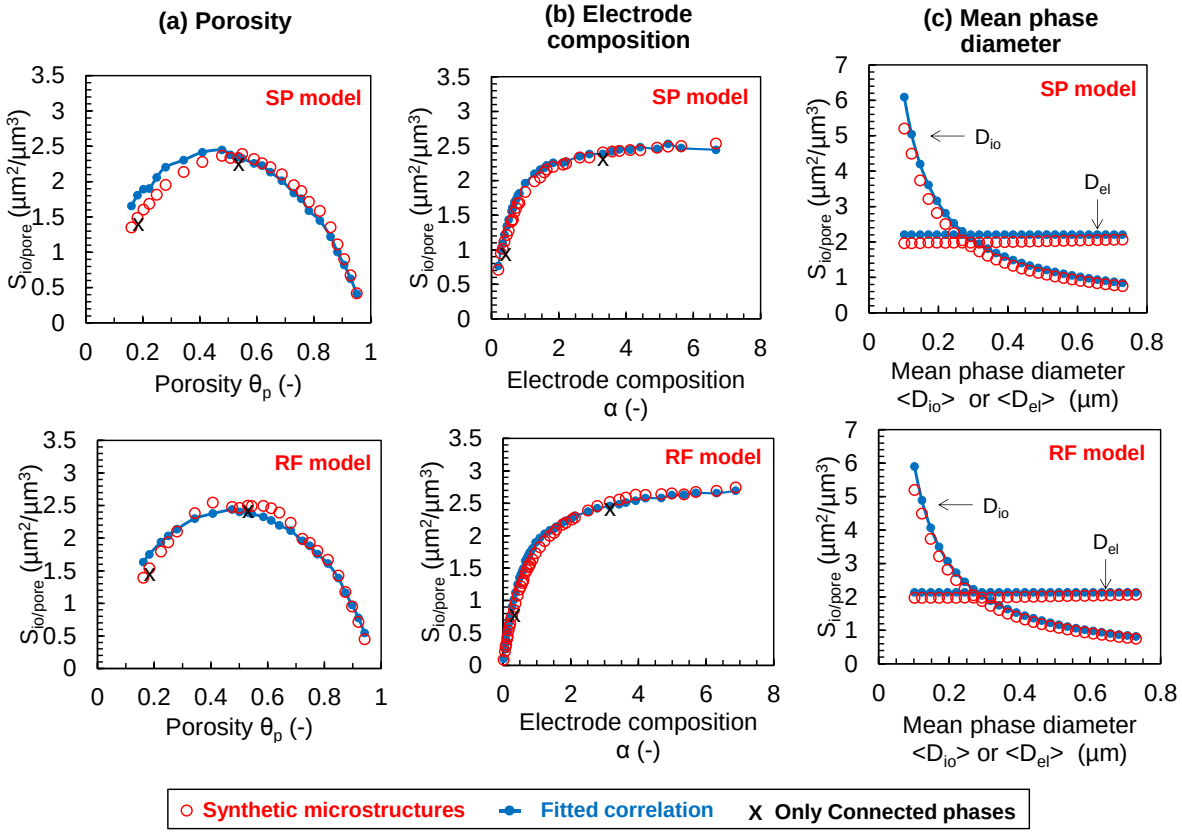

Fig. 3: Comparison between the interfacial specific surface area $S_{io/p}$ calculated with the correlation (16b) and the data measured on the 3D volumes generated by the RF and SP models. The surface area $S_{io/p}$ is plotted versus the porosity (a), the electrode composition (b) and the mean phase diameters (c). The crosses indicate the values for $S_{io/p}$ calculated with (16b) considering only the connected phases (for θ_{Ni}, θ_{YSZ} or $\theta_p = 0.18$). The scaling parameter β_{io} in (16b) has been fitted to $\beta_{io}^{RF} = 3.369$ and $\beta_{io}^{SP} = 3.476$ on the RF and SP microstructures, respectively.

According to eq. (16b), the ionic/pores interfacial surface area is proportional to $S_{io/p} \propto -\theta_p ln[\theta_p]$ meaning that the property exhibits a maximum at intermediate porosities. This evolution is well retrieved by both SP and RF models as shown in Fig. 3a. This behavior is easily explained since the surface area tends to zero in the case of a dense or a highly porous medium. Moreover, the surface area $S_{io/p}$ is a function of the electrode composition with a

relation $S_{io/p} \propto \frac{\alpha}{1+\alpha} = \frac{\theta_{io}}{\theta_{el}+\theta_{io}}$ given in eq. (16b). As discussed for the porosity, this dependence is also rather well reproduced by the numerical data (Fig. 3b). It can also be noticed that the ionic/pore surface area increases with the ratio α up to reach a plateau. Indeed, the contact surface area between the ionic phase and the porosity must increase with increasing the ionic content in the electrode composition. Finally, regarding eq. (16b), $S_{io/p}$ must be independent on the mean diameter of the electronic conducting phase whereas it is inversely proportional to the mean diameter of the ionic phase. Both of these dependences are perfectly confirmed by the RF and SP numerical models (Fig. 3c). This behavior is explained since a very fine microstructure for the ionic network must result in a high ionic/pore surface area irrespective of the size of the electronic phase.

3.1.2 Electronic/pores interfacial specific surface area

Following the same procedure as $S_{io/p}$, the semi-analytical expression (16a) for the electronic/pores interfacial surface area $S_{el/pore}$ has been calibrated with the same database of numerical microstructures. Similarly to the previous property, a general good consistency has been found with the two datasets obtained with the RF and SP models. The reader is invited to refer to the supplementary for the plots of $S_{el/pore}$ as a function of θ_p, α and $\langle D_i \rangle$. It has been confirmed using the numerical dataset that $S_{el/pore}$ follows the same evolution with the porosity as $S_{io/pore}$. Besides, the electronic/pore surface area has been found to be inversely proportional to the mean electronic phase diameter as predicted by eq. (16a). Finally, it has also been checked that $S_{el/pore}$ is directly proportional to the relative volume fraction of the electronic phase in the solid (i.e. $\frac{1}{1+\alpha} = \frac{\theta_{el}}{\theta_{el}+\theta_{io}}$).

In order to summarize all the results, the ionic/pores and electronic/pores interfacial specific surface areas measured on the set of synthetic microstructures have been plotted as a function of the semi-analytical estimations in Fig. 4. In this representation, all the points are rather well aligned proving the reliability of the proposed correlation for both RF and SP models.

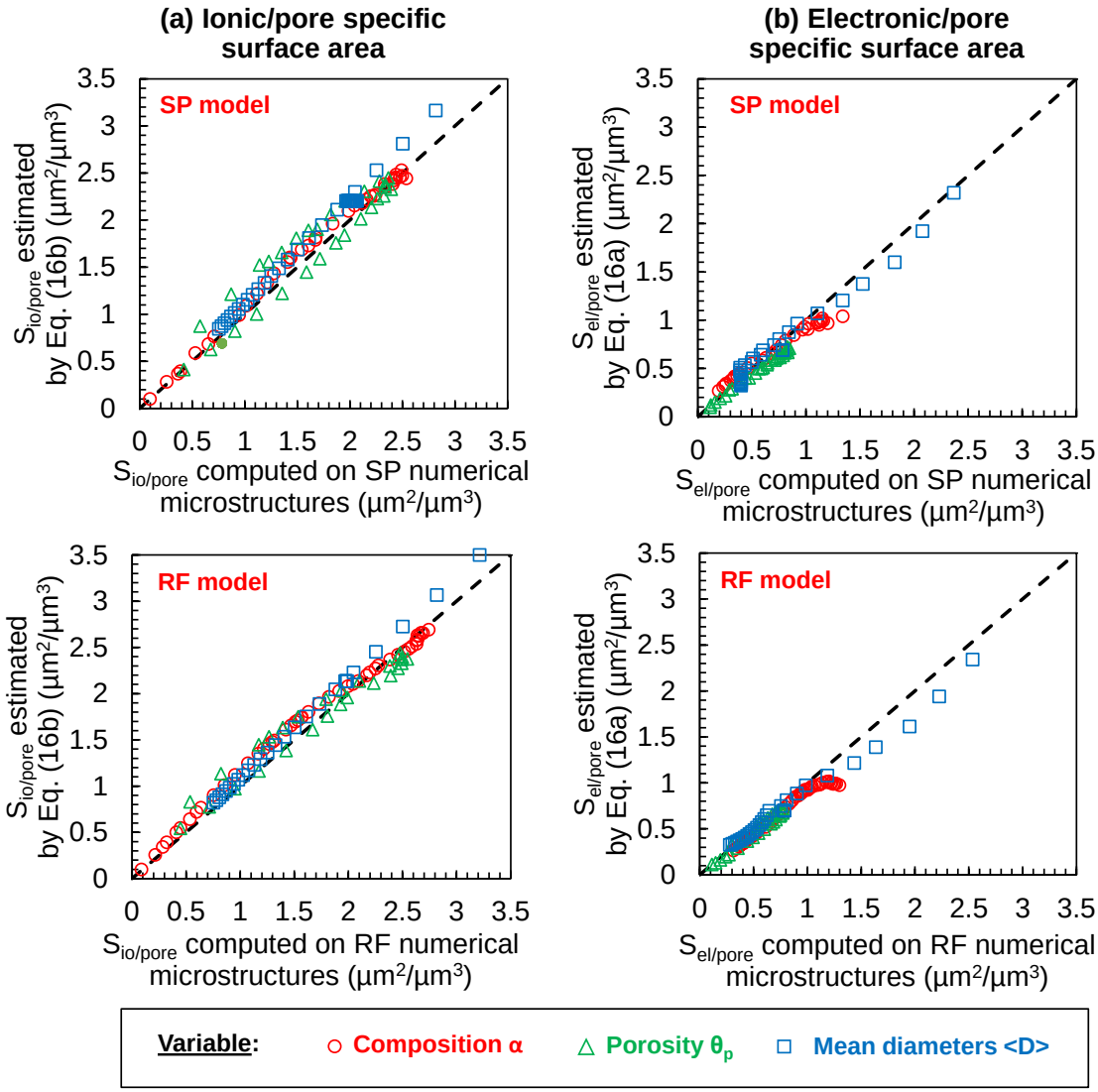

Fig. 4: Ionic/pores and electronic/pores interfacial specific surface areas estimated with the semi-analytical eqs. (16b) and (16a) are plotted as a function of the data measured on the set of RF and SP synthetic microstructures. The scaling parameters β_{io} and β_{el} have been fitted on the RF and SP microstructures to: $\beta_{io}^{RF} = 3.369$, $\beta_{io}^{SP} = 3.476$, and $\beta_{el}^{RF} = 2.476$, $\beta_{el}^{SP} = 2.454$.

3.2 Correlation for the electronic/ionic interfacial specific surface area

As shown in eq. (20), the expression of the electronic/ionic interfacial specific surface area is scaled by the product $\beta_{io} \times \beta_{el} \times a$. Knowing that β_{io} and β_{el} have already been determined on the previous relationships, only the scaling parameter a has been fitted for this correlation. The dependences of $S_{el/io}$ with the porosity, the composition and the mean phase diameters are shown in Fig. 5a, 5b and 5c. It can be seen that the proposed equation is able to predict accurately all the evolutions of the studied property measured on the synthetic microstructures

for both the RF and SP models. Moreover, in accordance with the previous relations for $S_{el/pore}$ and $S_{io/pore}$, it has been checked that the semi-analytical relation for $S_{el/io}$ is still valid for the percolated phases over the investigated range of microstructures (Fig. 5).

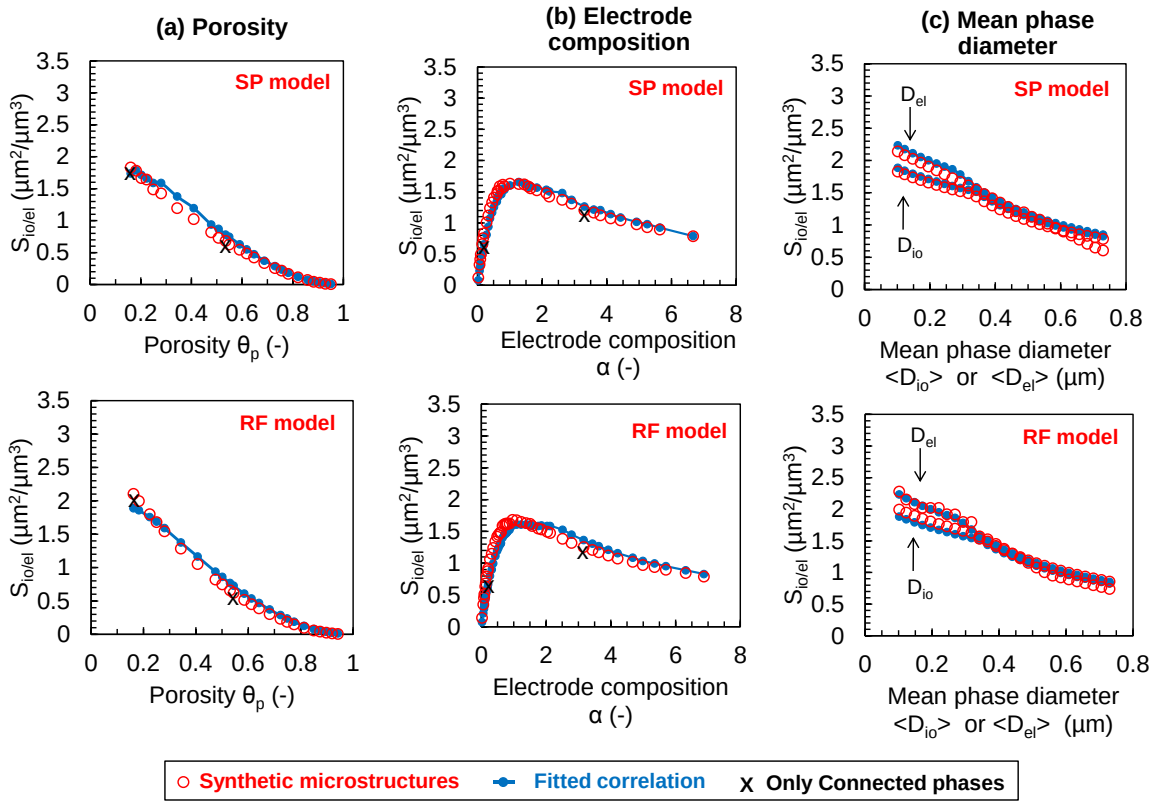

Fig. 5: Comparison between the specific interfacial surface area $S_{el/io}$ calculated with the correlation (20) and the data measured on the 3D dataset for the RF and SP models. The surface area $S_{el/io}$ is plotted versus the porosity (a), the electrode composition (b) and the mean phase diameters (c). The crosses indicate the values for $S_{el/io}$ calculated with (20) considering only the connected phases (for θ_{Ni}, θ_{YSZ} or $\theta_p = 0.18$). Correlation calibrated with $\beta_{io}^{RF} = 3.369$, $\beta_{el}^{RF} = 2.476$, $a^{RF} = 3.661$ and $\beta_{io}^{SP} = 3.476$, $\beta_{el}^{SP} = 2.454$ and $a^{SP} = 3.580$ on the RF and SP microstructures, respectively.

Unlike the specific surface area at electronic/pore or ionic/pore interfaces, the contact surface area between the two solid phases decreases continuously as a function of the porosity (Fig. 5a). Indeed, the volume fractions of both solid phases, and hence their contact, decreases when the microstructure is more porous. Besides, $S_{el/io}$ presents a maximum for $\alpha = 1$ when the amounts of ionic and electronic phases are equal (Fig. 5b).

As shown in eq. (20), the dependence of $S_{el/io}$ with the mean phase diameter is more complex than the one established for the surface area between the solid phases and the porosity. Indeed, the analytical correlation (20) predicts a coupled dependence in the mean diameters for both solid phases: $S_{el/io} \propto \frac{1}{\sqrt{\max\{\langle D_{el}\rangle,\langle D_{io}\rangle\}\times(\langle D_{io}\rangle+\langle D_{el}\rangle)}}$. Therefore, the electronic/ionic surface area must decrease when both mean diameters increase. More precisely, two regimes can be distinguished when changing one diameter (while the other remains constant in the sensitivity analysis). For instance, let one consider in Fig. 5c the case of changing $\langle D_{el}\rangle$ while $\langle D_{io}\rangle$ is kept constant to the reference value $\langle D_{io}\rangle$ =0.34 µm. If $\langle D_{el}\rangle > \langle D_{io}\rangle$, then the specific surface area is given by $S_{el/io} \propto \frac{1}{\sqrt{\langle D_{el}\rangle}\sqrt{\langle D_{el}\rangle+0.34}}$. Inversely, when $\langle D_{el}\rangle < \langle D_{io}\rangle$, the equation is reduced to $S_{el/io} \propto \frac{1}{\sqrt{\langle D_{el}\rangle+0.34}}$. This behavior predicted by the analytical model involves two slopes in the curve $S_{el/io} = f(\langle D_{el}\rangle)$ plotted in Fig. 5c. This evolution is perfectly reproduced by the data computed on the synthetic microstructures generated by the two models (Fig 5c). This result allows validating the mean diameters dependency depicted in eq. (20).

As expected, the error given by the correlation is minimum when the two mean diameters are similar in the sensitivity analysis (*i.e.* around the reference electrode for $\langle D_{io}\rangle \approx 0.34$ µm). Indeed, there is no approximation in the expression of the penetration length when the two diameters are equal as discussed in Section 2.2.4. Nevertheless, the error introduced when the two mean diameters differ from each other remains negligible as it can be seen in Fig. 5c. Consequently, the expression remains valid over a wide range of fine or coarse microstructures for the ionic or electronic phases.

All the results of the sensitivity analysis are reported in Fig. 6a. The values coming from the analytical correlation are compared to the numerical data measured on the 3D volumes for both SP and RF models. For all the dataset, the analytical predictions match all the values measured on the synthetic microstructures, highlighting the global consistency of the proposed correlations.

3.3 Correlation for the density of TPBl

The density of TPBl has been calculated with the correlation (4) by keeping the same scaling parameters β_{io} and β_{el} previously determined for the specific surface areas. In other words, no additional fitting parameter has been considered at this stage.

In this way, it has been found that the correlation (4) is able to accurately capture the TPBl evolutions as a function of the porosity, the electrode composition and the mean diameters of the electronic and ionic conducting phases measured on the synthetic microstructures (cf. supplementary). All the results are summarized in Fig. 6b where the densities of TPBl calculated with the semi-analytical correlation have been confronted to the data measured on the RF and SP synthetic microstructures. As shown in Fig. 6b, a good agreement is found between the analytical predictions and the numerical dataset, meaning that eq. (4) provides an accurate estimation of TPBl density for a large range of representative microstructures.

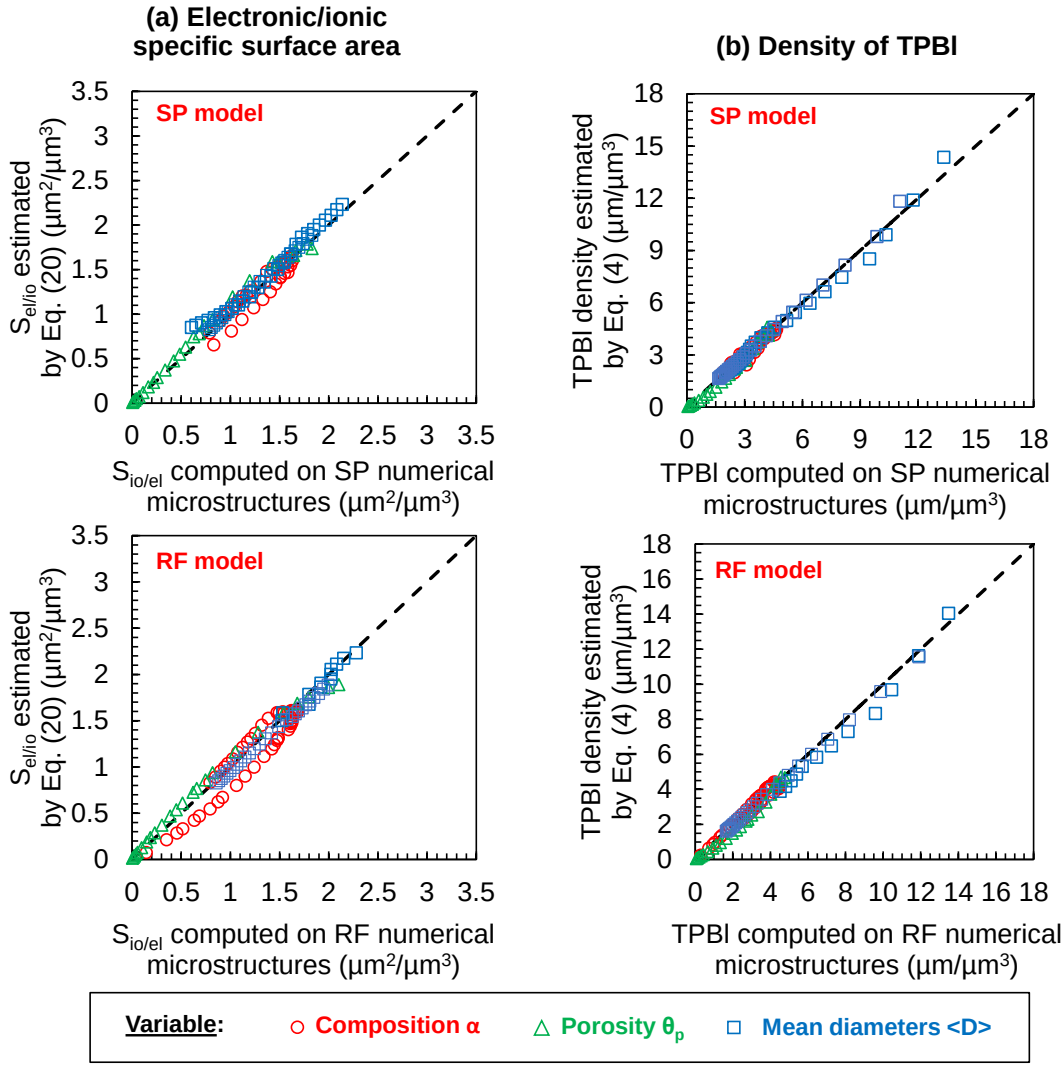

Fig. 6: Electronic/ionic interfacial specific surface area and density of TPBl estimated with the semi-analytical eqs (20) and (4) are plotted as a function of the data measured on the set of RF and SP synthetic microstructures. Correlation calibrated with $\beta_{io}^{RF} = 3.369$, $\beta_{el}^{RF} = 2.476$, $a^{RF} = 3.661$ and $\beta_{io}^{SP} = 3.476$, $\beta_{el}^{SP} = 2.454$ and $a^{SP} = 3.580$ on the RF and SP microstructures, respectively.

It is worth reminding that Zhang et al. [61] have already checked the validly of eq. (4) with simulated microstructures made of spherical powders or needle-shape particles (cf. Section 2.1). In their case, the electrode was thus composed by a collection of well-defined particles. Therefore, as predicted by the theory, it was possible to ascribe β_{io} and β_{el} to the shape of the constitutive element of the microstructures. In this work, it has been shown that the correlation can still be used for typical sintered SOCs electrodes with phases exhibiting a continuous and smooth shape (Fig. 2). However, in this particular case, it is reminded that the correlation is not fully analytical since β_{io} and β_{el}, which can no more be related to the particle shape, have to be considered as simple scaling parameters (without any geometrical meaning).

As done before with the interfacial specific surface areas, the active density of TPBl has been computed on the synthetic volumes by considering only the percolated phases. The dataset has been compared to the prediction of the semi-analytical correlation (4) depending on the phase volume fractions. The results are illustrated in Fig 7 changing the ionic content in the electrode. As mentioned for the specific surface area, it can be observed that eq. (4) is able to accurately predict the active TPBl as long as the electrode phases are well connected. Indeed, it has been found that the TPBl calculated with eq. (4) matches the data measured on the percolated microstructures as long as each volume fraction is higher than ≈18 %. It can be noticed that the condition to calculate the active density of triple-phase boundary is more restrictive than the one requested for the specific surface area. Indeed, the three electrode phases have to be connected at the same time for the active TPBls whereas only two are necessary for $S_{i/j}$.

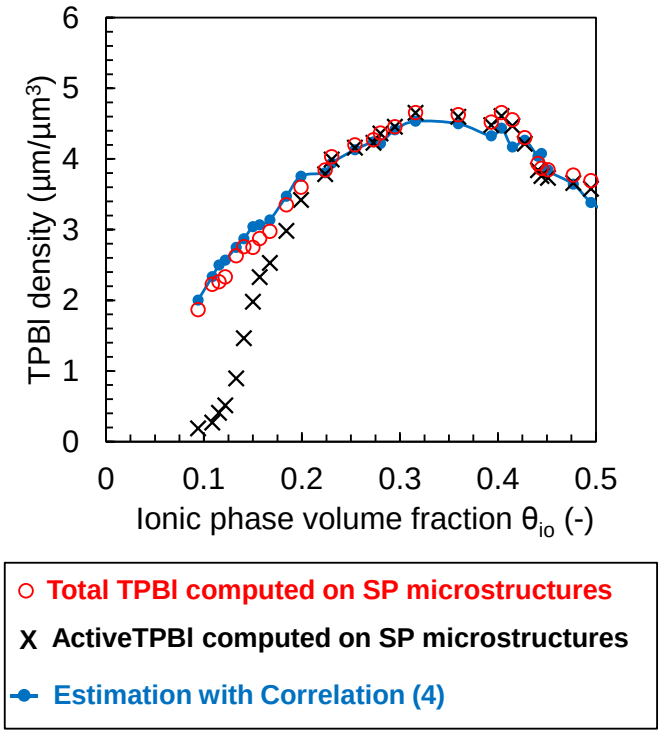

Fig. 7: Comparison between the density of TPBl calculated with the correlation (4) and the ones measured on the total and connected phases on the SP synthetic microstructures as a function of the ionic content in the electrode ($\beta_{io}^{SP} = 3.476$, $\beta_{el}^{SP} = 2.454$).

4. Discussion and validation

The consistency of the calibrated correlations with respect to the RF and SP models are discussed as a first element of validation. The final check-up of the model reliability is then conducted by comparing the predictions with the properties measured on the real electrodes reconstructions.

4.1 Model prediction with respect to the RF and SP microstructures

The calibration of the previous correlations for $S_{i/j}$ and TPBl has been carried out on two sets of representative synthetic microstructures generated by two fundamentally different mathematical models. In spite of the large range of investigated cases in the sensitivity analyses, it has been shown that the semi-analytical equations are able to capture all the microstructural evolutions with only three fitting parameters. This preliminary remark constitutes a first evidence for the model validation.

Moreover, the scaling parameters are equal to $\beta_{io}^{RF} = 3.369$, $\beta_{el}^{RF} = 2.476$ and $a^{RF} = 3.661$ for the correlations calibrated on the dataset coming from the random field microstructures. By using the sphere packing algorithm, the fitting parameters have been estimated to $\beta_{io}^{SP} = 3.476$, $\beta_{el}^{SP} = 2.454$ and $a^{SP} = 3.580$. Therefore, it can be claimed that there is a very good consistency between the two sets of scaling parameters fitted on the RF and SP microstructures. It is worth reminding that the two numerical models, which have been validated on one single electrode reconstruction, must provide two approximations of the real electrodes when changing the 'basic' parameters of the microstructure such as the porosity. From that point of view, the two sets of calibrated semi-analytical correlations should converge toward two independent estimations of the reality. As the scaling parameters are very close to each other, it means that the two predictions remain fully coherent when considering the two approximations given by the RF and SP models. As a consequence, the semi-analytical correlations should provide two accurate predictions over a large range of real electrodes microstructures. In order to check this assertion, the predictions of the correlations have been compared to the properties measured on various electrode reconstructions.

4.2 Model validation on diverse electrodes reconstructions

In Table I, the properties measured on the reconstructions of electrode_1, electrode_2 and electrode_3 (Fig. 2a) are compared to the data calculated with the semi-analytical correlations. As a general comment, it can be seen that a good agreement is found between the properties measured on the 3D volumes and the ones calculated with the calibrated semi-analytical equations. Indeed, whatever the electrodes or the calculated properties, the error on the parameters estimations does not exceed 12% with an average of 5.4%. More precisely, the inspection of the data reported in Table I reveals that the correlations calibrated on the SP and RF microstructures provide in average almost the same estimation with respect to the real electrode properties (mean error of 5.5% and 5.3% for the SP and RF models, respectively). Therefore, the difference in the parameters coming from the two calibrations on the RF and SP microstructures is quite negligible, confirming that both sets of correlations provide a good approximation of the reality.

Table I. Comparison between the properties measured on the 3D reconstructions and the predictions given by the correlations.

	L_{TPB} (µm^{-2})			$S_{io/el}$ (µm^{-1})		
	Measured on the reconstruction	Correlation (4) calibrated with SP model	Correlation (4) calibrated with RF model	Measured on the reconstruction	Correlation (20) calibrated with SP model	Correlation (20) calibrated with RF model
Electrode_1 (Ni_YSZ)	4.75	4.28 (Error=-9.8%)	4.19 (Error=-11.8%)	1.59	1.59 (Error=+0.0%)	1.59 (Error=+0.0%)
Electrode_2 (Ni-YSZ)	5.46	5.19 (Error=-5.0%)	5.07 (Error=-7.1%)	1.85	1.83 (Error=-0.9%)	1.83 (Error=-1.0%)
Electrode_3 (LSCF-CGO)	8.78	8.12 (Error=-7.5%)	7.94 (Error=-9.5%)	1.65	1.67 (Error=+1.2%)	1.67 (Error=+1.2%)
	$S_{io/pore}$ (µm^{-1})			$S_{el/pore}$ (µm^{-1})		
	Measured on the reconstruction	Correlation (16b) calibrated with SP model	Correlation (16b) calibrated with RF model	Measured on the reconstruction	Correlation (16a) calibrated with SP model	Correlation (16a) calibrated with RF model
Electrode_1 (Ni_YSZ)	2.01	2.20 (Error=+9.7%)	2.14 (Error=+6.4%)	0.63	0.69 (Error=+9.9%)	0.70 (Error=+10.9%)
Electrode_2 (Ni-YSZ)	1.75	1.87 (Error=+7.0%)	1.81 (Error=+3.7%)	0.89	0.94 (Error=+5.2%)	0.94 (Error=+6.1%)
Electrode_3 (LSCF-CGO)	2.12	2.24 (Error=+6.0%)	2.18 (Error=+2.7%)	2.09	2.01 (Error=-3.8%)	2.03 (Error=-2.9%)

The semi-analytical equations are thus able to accurately predict the properties for the typical Ni-YSZ cermets of Electrode_1 and Electrode_2 as well as for the LSCF-CGO composite of Electrode_3. In the latter case, the electrode microstructure is much finer than the two cermets with lower mean diameters for the ionic and electronic conducting phases (cf. microstructures displayed in Fig. 2a with $\{\langle D_{LSCF}\rangle = 0.17\ \mu m;\ \langle D_{CGO}\rangle = 0.16\ \mu m$ for Electrode_3$\} < \{\langle D_{Ni}\rangle = 0.34\ \mu m, \langle D_{YSZ}\rangle = 0.28\ \mu m$ for Electrode_1$\}$). This finer microstructure for Electrode_3 results in a significantly higher density of TPBl that is well captured by the semi-analytical relation. As a conclusion, it can be inferred from this analysis that the proposed correlations are able to accurately predict the density of TPBl and the interfacial surface areas for different kinds of SOC electrodes (manufactured by the classical manufacturing routes for ceramics).

4.3 Model validation on the loss of TPBl after Ni agglomeration

For Electrode_1, some reconstructions have been also acquired after ageing at 850°C. The experimental conditions of the long-term testing and the microstructural characterization have been detailed in [25]. It was found that the Ni phase undergoes a substantial particle coarsening in operation that was modeled by a standard Ostwald ripening power-law equation:

$$[\langle D_{Ni}(t)\rangle^n - \langle D_{Ni}(t=0)\rangle^n] = k_{pow} \times t \quad (21)$$

where t is the time, k_{pow} the rate constant and n an exponent which is characteristic of the predominant mass transport in the sintering process. The grain-size growth in the cermet was measured on the reconstructed electrodes and the best adjustment of eq. (21) on the experimental data was found for $n = 8$. It was also highlighted that the Ni phase coarsening leads to a substantial decrease in TPBl whereas the volume fractions and the mean phase diameters for the complementary phases remain quite unaffected by the agglomeration.

To check the possibility to use the present microstructural modeling to reproduce the loss of TPBl, eq. (21) has been combined with the correlation (4) calibrated with the SP microstructures. Without any supplementary fitting, the loss of TPBl given by the semi-analytical relations (4) and eq. (21) is compared in Fig. 8 to the values measured on the reconstructions. Even if the scattering on the experimental data is rather significant, the two equations are able to predict the evolution of TPBl over the time. This result brings a supplementary evidence on the reliability of the correlation. Besides, it can be mentioned that the system of eqs. (4) and (21) constitutes a physically-based model to compute the loss of TPBl induced by the Ni agglomeration.

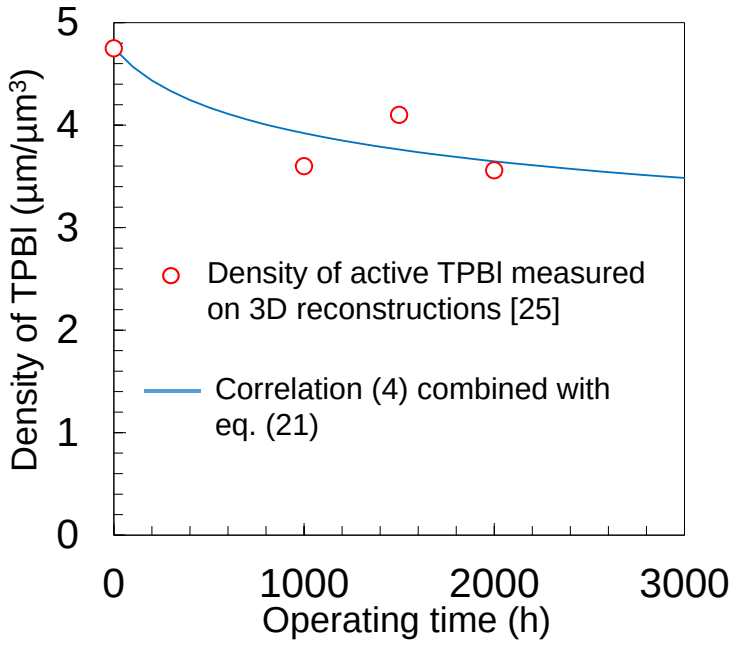

Fig. 8: Comparison between the loss of active TPBl measured on several 3D reconstructions after operation and the prediction combining the correlation (4) with the power-law model (21) for the Ni particle coarsening ($\beta_{io}^{SP} = 3.476$, $\beta_{el}^{SP} = 2.454$).

Finally, some authors have also investigated the evolution of the cermet microstructural properties before and after Ni agglomeration by 3D electrode reconstructions [22,67]. For instance, Faes et al. [22] have reported a percentage decrease of 25% in the density of TPBl (after 1130h for 'Stack A') whereas Lee et al. [67] have found, in their experimental conditions, a percentage drop of 55% (after 50h at 1200°C). The change in the 'basic' microstructural parameters provided in the two articles have been used to calculate the TPBls decrease with the correlation (4). The model leads to an estimation of the percentage loss of 26% and 50% (instead of 25% and 55%, respectively). The good agreement between the published data and the estimated values also highlights the model validity.

5. Conclusion

The concept of "extended" microstructure has been applied to express the correlations relating the key microstructural properties, which control the electrochemistry, to the 'basic' parameters of the microstructure. This approach was initially employed in [35] to establish the relation linking the density of TPBl as a function of (i) the porosity, (ii) the electrode composition, (iii) the geometrical shape and size distribution of particles for the electronic and ionic conducting phases. Following the same approach, the method has been applied in the present work to derive the equations for the ionic/pore, electronic/pore and ionic/electronic interfacial specific surface areas.

The correlations have been studied for the classical SOCs electrodes for which the phases exhibit a continuous shape without remanence of the initial powder particles after sintering. In that case, the three parameters associated to the geometry of the particles and their contacts in the final microstructure have been considered as simple scaling factors.

These scaling parameters have been determined by fitting the semi-analytical relations on a large dataset of properties measured on representative synthetic microstructures generated by two different mathematical methods (i.e. the Gaussian Random Field and the Sphere Packing models). In both cases, the semi-analytical correlations have been found to capture all the evolutions in terms of porosity, electrode composition and mean phase diameters. As long as the phases are well percolated (i.e. for volume fractions higher than ≈18%), it has been found that the correlations remain valid.

The validity of the calibrated correlations has been discussed with respect to the two numerical methods used for the microstructural generation. It has been shown that the correlations were able to accurately fit the two datasets that provide two independent but close estimations of the real microstructures. To go further in the model validation, the properties calculated by the semi-analytical equations have been also compared to the data measured on several 3D electrode reconstructions. It has been found that the correlations provide accurate predictions for typical Ni-YSZ cermets and LSCF-CGO composite electrodes. Indeed, the estimated average on the error between the estimated properties and the real data are lower than 5.4%, demonstrating the reliability of the proposed semi-analytical correlations. Finally, it has also been shown that the TPBl correlation combined with a power-law model describing the particle growth due to Ni coarsening is able to capture the loss of active TPBl in operation.

Acknowledgement

The research leading of these results has received funding from the European Horizon 2020 – Research and Innovation Framework program (H2020-JTI-FCH-2015-1) under grant agreement n°735918 (INSIGHT project) and n°699892 (ECO project). The work has also been partially supported by the French National Agency (ANR) (ECOREVE project) and the Carnot Institute Energies du Futur (DURASOC project).

References

[1] A. Godula-Jopek, “Hydrogen Production by Electrolysis”, Wiley, 2015.

[2] C. Graves, S.D. Ebbesen, S.H. Jensen, S.B. Simonsen, M.B. Mogensen, Nature Materials, 14 (2015) 239-244.

[3] S.C. Singhal and K. Kendall, “High Temperature Solide Oxide Fuel cells, Fundamental, Design and Applications”, Elsevier, 2003.

[4] V. Dusastre, J.A. Kilner, Optimisation of composite cathodes for intermediate temperature SOFC applications, Solid State Ionics, 126 (1999) 163-174.

[5] Y.T. Kim, Z. Jiao, N. Shikazono, Evaluation of $La_{0.6}Sr_{0.4}Co_{0.2}Fe_{0.8}O_3$-$Gd_{0.1}Ce_{0.9}O_{1.95}$ composite cathode with three dimensional microstructure reconstruction, J. Power Sources, 342 (2017) 787-795.

[6] Y.T. Kim, N. Shikazono, Investigation of $La_{0.6}Sr_{0.4}CoO_{3-\delta}$-$Gd_{0.1}Ce_{0.9}O_{1.95}$ composite cathode with different volume ratios by three dimensional reconstruction, Solid State Ionics, 309 (2017) 77-85.

[7] Y. Leng, S. Hwa Chan, Q. Liu, Development of LSCF-GDC composite cathodes for low-temperature solid oxide fuel cells with thin film GDC electrolyte, Int. J. Hydrogen Energy, 33 (2008) 3808-3818.

[8]J. Hanna, W.Y. Lee, Y. Shi, A.F. Ghoniem, Fundamentals of electro- and thermochemistry in the anode of solid-oxide fuel cells with hydrocarbon and syngas fuels, Progress in Energy and Combustion Science, 40 (2014) 74-111.

[9] B. Shri Prakash, S. Senthil Kumar, S.T. Aruna, Properties and development of Ni/YSZ as an anode material in solid oxide fuel cell: A review, Renewable and Sustainable Energy Reviews, 36 (2014) 149–179.

[10] H. Abe, K. Murata, T. Fukui, W.-J. Moon, K. Kaneko, M. Naito, Microstructural control of Ni–YSZ cermet anode for planer thin-film solid oxide fuel cells, 496 (2006) 49-52.

[11] M. Ostergard, C. Clausen, C. Bagger, M. Mogensen, Manganite-zirconia composite cathodes for SOFC: influence of structure and composition, Electrochimica Acta, 40 (12) (1995) 1971-1981.

[12] Toshio Suzuki, Z. Hasan, Y. Funahashi, T. Yamaguchi, Y. Fujishiro, M. Awano, Impact of Anode Microstructure on Solid Oxide Fuel Cells, Science, 325 (2009) 852-855.

[13] A.V. Virkar, J. Chen, C.W. Tanner, J.-W.Kim, the role of electrode microstructure on activation and concentration polarizations in solid oxide fuel cells, Solid State Ionics, 131 (2000) 189-98.

[14] F. Usseglio-Viretta, J. Laurencin, G. Delette, J. Villanova, P. Cloetens, Quantitative microstructure characterization of a Ni-YSZ bi-layer coupled with simulated cathode polarisation, J. Power Sources, 256 (2014) 394-403.

[15] M. Hubert, J. Laurencin, P. Cloetens, J.C. Da Silva, F. Lefebvre-Joud, P. Bleuet, A. Nakajo, E. Siebert, Role of microstructure on electrode operating mechanisms for mixed ionic electronic conductors: From synchrotron-based 3D reconstruction to electrochemical modelling, Solid State Ionics, 294 (2016) 90-107.

[16] J. Laurencin, M. Hubert, K. Couturier, T. Le Bihan, P. Cloetens, F. Lefebvre-Joud, E. Siebert, Reactive Mechanisms of LSCF Single-Phase and LSCF-CGO Composite Electrodes Operated in Anodic and Cathodic Polarisations, Electrochimica Acta, 174 (2015) 1299-1316.

[17] S.B. Adler, J.A. Lane, B.C.H. Steele, Electrode Kinetics of Porous Mixed-Conducting Oxygen Electrodes, J. Electrochem. Soc. 143 (1996) 3554-3564.

[18] F. Monaco, V. Tezyk, E. Siebert, S. Pylypko, B. Morel, J. Vulliet, T. Le Bihan, F. Lefebvre-Joud, J. Laurencin, Experimental validation of a La0.6Sr0.4Co0.2Fe0.8O3-δ electrode model operated in electrolysis mode: Understanding the reaction pathway under anodic polarization, Solid State Ionics, 319 (2018) 234-246.
[19] John T. S. Irvine, Dragos Neagu, Maarten C. Verbraeken, Christodoulos Chatzichristodoulou, Christopher Graves & Mogens B. Mogensen, Evolution of the electrochemical interface in high-temperature fuel cells and electrolysers, Nature Energy, 1 (2016) 1-13.
[20] E. Lay-Grindler, J. Laurencin, G. Delette, J. Aicart, M. Petitjean, L. Dessemond, Micro-modelling of Solid Oxide Electrolysis Cell: from performance to durability, Int. J. of Hydrogen Energy, 38 (2013) 6917-6929.
[21] P. Moçoteguy, A. Brisse, A review and comprehensive analysis of degradation mechanisms of solid oxide electrolysis cells, Inter. J. Hydrogen Energy, 38 (2013) 15887-15902.
[22] A. Faes, A. Hessler-Wyser, D. Presvytes, C. G. Vayenas, Nickel–zirconia anode degradation and triple phase boundary quantification from microstructural analysis, Fuel cells 9(6) (2009) 841-851.
[23] Z. Jiao, N. Shikazono, N. Kasagi, Quantitative Characterization of SOFC Nickel-YSZ Anode Microstructure Degradation Based on Focused-Ion-Beam 3D-Reconstruction Technique, J. Electrochem. Soc., 159 (3) (2012) B285-B291.
[24] E. Lay-Grindler, J. Laurencin, J. Villanova, P. Cloetens, P. Bleuet, A. Mansuy, J. Mougin, G. Delette, Degradation study by 3D reconstruction of a nickel-yttria stabilized zirconia cathode after high temperature steam electrolysis operation, Journal of Power Sources 269 (2014) 927-936.
[25] M. Hubert, J. Laurencin, P. Cloetens, B. Morel, D. Montinaro, F. Lefebvre-Joud, Impact of Nickel agglomeration on solid oxide cell operated in fuel cell and electrolysis modes, J. Power Sources, 397 (2018) 240-251.
[26] J.S. Cronin, Y.C.K. Chen-Wiegart, J. Wang, S.A. Barnett, Three-dimensional reconstruction and analysis of an entire solid oxide fuel cell by full-field transmission X-ray tomography, J. Power Sources 233 (2013) 174–179.
[27] K.N. Grew, Y.S. Chu, J. Yi, A.A. Peracchio, J.R. Izzo, Y. Hwu, F. De Carlo, W.K. Chiu, Nondestructive nanoscale 3D elemental mapping and analysis of a solid oxide fuel cell anode, J. Electrochem. Soc., 157 (6) (2010) B783–B792.
[28] M. Hubert, A. Pacureanu, C. Guilloud, Y. Yang, Julio C. da Silva, J. Laurencin, F. Lefebvre-Joud, Peter Cloetens, Efficient correction of wavefront inhomogeneities in X-ray holographic nanotomography by random sample displacement, Applied Physic Letters, 112 (2018) 203704 1-5.
[29] P.R. Shearing, R.S. Bradley, J. Gelb, F. Tariq, P.J. Withers, N.P. Brandon, Exploring microstructural changes associated with oxidation in Ni–YSZ SOFC electrodes using high resolution X-ray computed tomography, Solid State Ionics, 216 (2012) 69–72.
[30] J. Villanova, J. Laurencin, P. Cloetens, P. Bleuet, G. Delette, H. Suhonen, F. Usseglio-Viretta, 3D phase mapping of SOFC YSZ/Ni cermet at the nanoscale by X-Ray holotomography, J. Power Sources 243 (2013) 841–849.
[31] L. Holzer, B. Münch, B. Iwanschitz, M. Cantoni, T. Graule, Quantitative relationships between composition, particle size, triple phase boundary length and surface area in nickel-cermet anodes for solid oxide fuel cells, J. Power Sources 196 (2011) 7076–7089.

[32] N. Vivet, S. Chupin, E. Estrade, T. Piquero, P.L. Pommier, D. Rochais, E. Bruneton, 3D Microstructural characterization of a solid oxide fuel cell anode reconstructed by focused ion beam tomography, J. Power Sources. 196 (2011) 7541–7549.
[33] J.R. Wislon, W. Kobsiriphat, R. Mendoza, H.Y. Chen, J.M. Hiller, D.J. Miller, K. Thorton, P.W. Voorhees, S.B. Adler, S.A. Barnett, Three –dimensional reconstruction of solid-oxide fuel-cell anode, Nat. Mater. 5 (2006) 541–544.
[34] D. Chen, H. He, D. Zhang, H. Wang, M. Ni, Percolation theory in solid oxide fuel cell composite electrodes with a mixed electronic and ionic conductor, Energies, 6 (2013) 1632-1656.
[35] A.M. Gokhale, S. Zhang, M. Liu, A stochastic geometry model for total triple phase boundary length in composite cathodes for solid oxide fuel cells, J. Power Sources, 194 (2009) 303–312.
[36] A. Ali, X. Wen, K. Nandakumar, J. Luo, K.T. Chuang, Geometrical modeling of microstructure of solid oxide fuel cell composite electrodes, J. Power Sources, 185 (2008) 961-966.
[37] A. Bertei, H.-W. Choi, J.G. Pharoah, C. Nicolella, Percolating behavior of sintered random packings of spheres, Powder Tech., 231 (2012) 44-53.
[38] Q. Cai, C.S. Adjiman, N. Brandon, Modelling the 3D microstructure and performance of solid oxide fuel cell electrodes: computational parameters, Electrochimica Acta, 56 (2011) 5804-5814.
[39] B. Kenney, M. Valdmanis, C. Baker, J.G. Pharoah, K. Karan, Computation of TPB length, surface area and pore size from numerical reconstruction of composite solid oxide fuel cell electrodes, J. Power Sources, 189 (2009) 1051-1059.
[40] C. Metcalfe, O. Kesler, T. Rivard, F. Gitzhofer, N. Abatzoglou, Connected three-phase boundary length evaluation in modeled sintered composite solid oxide fuel cell electrodes, J. Electrochem. Soc., 157(9) (2010) B1326-B1335.
[41] H. Moussaoui, J. Laurencin, Y. Gavet, G. Delette, M. Hubert, P. Cloetens, T. Le Bihan, J. Debayle, Stochastic Geometrical Modeling of Solid Oxide Cells Electrodes Validated on 3D Reconstructions, Computational Materials Science, 143 (2018) 262-276.
[42] M. Neumann, J. Staněk, O.M. Pecho, L. Holzer, V. Beneš, V. Schmidt, Stochastic 3D modeling of complex three-phase microstructure in SOFC electrodes with completely connected phases, Comput. Mater. Sci., 118 (2016) 353-364.
[43] Y. Suzue, N. Shikazono, N. Kasagi, Micro modeling of solid oxide fuel cell anode based on stochastic reconstruction, J. Power Sources, 184 (2008) 52-59.
[44] A. Bertei, C. Nicolella, Percolation theory in SOFC composite electrodes: effects of porosity and particle size distribution on effective properties, J. Power Sources, 196 (2011) 9429-9436.
[45] S.H. Chan, X.J. Chen, K.A. Khor, Cathode micromodel of solid oxide fuel cell, J. Electrochem. Soc., 151 (2004) A164-A172.
[46] D. Chen, L. Lu, J. Li, Z. Yua, W. Kong, H. Zhu, Percolation micro-model to predict the effective properties of the composite electrode with poly-dispersed particle sizes, J. Power Sources 196 (2011) 3178-3185.
[47] P. Costamagna, P. Costa, V. Antonucci, Micro-modelling of solid oxide fuel cell electrodes, Electrochimica Acta, 43 (1998) 375-394.
[48] V.J. Janardhanan, V. Heuveline, O. Deutschmann, Three-phase boundary length in solid-oxide fuel cells: a mathematical model, J. Power Sources, 178 (2008) 368-372.

[49] S. Sunde, Simulations of composite electrodes in fuel cells, Journal of Electroceramics, 5, (2000) 153-182.
[50] S. Sunde, Monte Carlo simulations of polarization resistance of composite electrodes for solid oxide fuel cells, J. Electrochem. Soc., 143 (1996) 1930-1939.
[51] Y. Zhang, Y. Wang, Y. Wang, F. Chen, C. Xia, Random-packing model for solid oxide fuel cell electrodes with particles size distributions, J. Power Sources, 196 (2011) 1983-1991.
[52] S. Zhang, Quantitative characterization and modelling of the microstructure of solid oxide fuel cell composite electrodes, Ph.D. dissertation, School of Materials Science and Engineering, Georgia Institute of Technology, Atlanta (2010).
[53] O. Stenzel, O. Pecho, L. Holzer, M. Neumann, V. Schmidt, Big data for microstructure-property relationships: a case study of predicting effective conductivities, AIChE Journal, 63 (2017) 4224-4232.
[54] M. Avrami, Kinetics of Phase Change. I: General Theory, The Journal of Chem. Phys., 7 (1939) 1103-1112.
[55] M. Avrami, Kinetics of Phase Change. II: Transformation-Time Relations for Random Distribution of Nuclei, The Journal of Chem. Phys., 8 (1940) 212-224.
[56] M. Avrami, Kinetics of Phase Change. III: Granulation, Phase Change, and Microstructure, The Journal of Chem. Phys., 9 (1941) 177-184.
[57] M. Fanfoni, M. Tomellini, The Johnson-Mehl-Avrami-Kohnogorov model: A brief review, Il Nuovo Cimento, 20D (1998) 1171-1182.
[58] A.M. Gokhale, C.V. Iswaran, R.T. Dehoff, Application of microstructure modelling to the kinetics of recrystallization, Metall. Trans. A, 11A (1980) 1377-1383.
[59] A.M. Gokhale, A test for randomness of the spatial distribution of particles during phase transformation, Metall. Trans. A, 15A (1984) 243-245.
[60] S.J. Jones, H.K.D.H. Bhadeshia, Kinetics of the simultaneous decomposition of austenite into several transformation products, Acta Mater. 45 (1997) 2911-2920.
[61] S. Zhang, A.M. Gokhale, Computer simulations of topological connectivity of the triple phase boundaries in solid oxide fuel cell composite cathodes, J. Power Sources, 219 (2012) 172-179.
[62] S. Amitai, A. Bertei, R. Blumenfeld, Theory-based design od sintered granular composite triples three-phase boundary in fuel cells, Physical review E, 96 (2017) 052903 1-10.
[63] J. Serra, Image analysis and mathematical morphology: Theoretical advances, Academic Press, Cornell University, 1988.
[64] H. Moussaoui, J. Laurencin, G. Delette, Y. Gavet, M. Hubert, P. Cloetens, J. Debayle, To be submitted, J. Power Sources (2019).
[65] J. Laurencin, R. Quey, G. Delette, H. Suhonen, P. Cloetens, P. Bleuet, Characterisation of SOFC Ni-8YSZ substrate by synchrotron X-ray nano-tomography. From 3D reconstruction to microstructure quantification, J. Power Sources 198 (2012) 182-189.
[66] L.D. Gelb, K.E. Gubbins, Pore size distributions in porous glasses: a computer simulation study, Langmuir, 15 (1999) 305-308.
[67] Y.H. Lee, H. Muroyama, T. Matsui, K. Eguchi, Degradation of nickel–yttria-stabilized zirconia anode in solid oxide fuel cells under changing temperature and humidity conditions, 262 (2014) 451-456.

List of symbols

Roman symbols

a	Scaling parameter in the correlations for $S_{io/el}$	(-)
$\langle d_c \rangle$	Mean value of the contact diameter between the ionic and electronic particles	(m)
$\langle D_i \rangle$	Mean particle diameter	(m)
k_{pow}	Rate constant for Ni coarsening	($m^8.s^{-1}$)
K_{1i}	Shape factor for the surface area	(-)
K_{2i}	Shape factor for the volume	(-)
ℓ	Penetration length between two particles	(m)
L_{TPB}	Density of total TPBl	(m^{-2})
n	Exponent in the power law model for Ni coarsening	(-)
N_i	Number of ionic or electronic particles per unit volume	(m^{-3})
N_c	Number of ionic and electronic contacts per unit volume	(m^{-3})
S_i	Specific surface area for i	(m^{-1})
$S_{i/j}$	Interfacial specific surface area between i and j	(m^{-1})
S_i^{ex}	Specific surface area in the extended microstructure for i	(m^{-1})
$\langle S_i \rangle$	Mean surface area of the electronic or ionic particles	(m^2)
t	Time	(s)
V_i	Volume of the phase i	(m^3)
$\langle V_i \rangle$	Mean volume of the electronic or ionic particles	(m^3)
V_i^{ex}	Volume of the phase i in the extended microstructure	(m^3)
V_{tot}	Total volume of the domain	(m^3)

Greek symbols

α	Ratio of the ionic to the electronic phase volume fractions	(-)
β_i	Ratio of shape factors/scaling parameters in the semi-analytical correlations	(-)
γ_i	Skewness of the PSD_i	(-)
θ_i	Phase volume fraction	(-)

Subscript

$i \ (or\ j)$	Electrode phase: i=ionic (io), electronic (el), porosity (p)	(-)

List of abbreviations

CGO	Ceria doped Gadolinium Oxide
CV_i	Coefficient of Variation of the PSD_i
FIB-SEM	Focused Ion Beam-Scanning Electron Microscopy
PSDi	Particle Size Distribution
LSCF	Lanthanum Strontium Cobalt Ferrite
MIEC	Mixed Electronic and Ionic Conductor
RF	Random Field
SOCs	Solid Oxide Cells
SOEC	Solid Oxide Electrolysis Cell
SOFC	Solid Oxide Fuel Cell
SP	Sphere-Packing
TPBl	Triple Phase Boundary lengths
YSZ	Yttria Stabilized Zirconia